Journal of The Electrochemical Society, **160** (6) H360-H367 (2013)
0013-4651/2013/160(6)/H360/8/$31.00 © The Electrochemical Society

Electrochemical Characteristics of Closely Spaced Defect Tuned Carbon Nanotube Arrays

M. Hoefer and P. Bandaru[z]

Materials Science Program, Department of Mechanical Engineering, University of California, San Diego, La Jolla, California 92093, USA

The ability to understand the role of defects in nanostructures, such as carbon nanotubes (CNTs), is crucial for determining their utility in many applications. We analyze the improvement in electrochemical performance of multi-walled CNT arrays that were exposed to argon and hydrogen based plasmas, where it was hypothesized that locally charged defects could be created through exposure to ions in the plasma. Such defects would influence the graphitic structure and were monitored through Raman spectroscopy. Cyclic voltammetry and associated electrochemical techniques were employed to infer the effects of plasma exposure on electrochemical charge transfer. It was seen that the effective area of charge transfer could be reproducibly increased through argon plasma exposure by ∼100%, while exposure to hydrogen based plasmas resulted in decrease in the effective area by nearly 60%, under the investigated conditions. Our experiments indicate enhanced faradaic currents, involving non-planar diffusion processes of the electroactive species, with implications for enhanced charge and energy storage.
 [DOI: 10.1149/2.122306jes]

Manuscript submitted February 7, 2013; revised manuscript received April 2, 2013. Published April 10, 2013.

The need for high energy density materials continually increases with the proliferation of portable electronics and energy harvesting devices. In this article, we present principles and methodologies, through which the energy density of electrochemical devices can be further enhanced, and thus applicable to the design of new generations of battery[1,2] and capacitor[3–5] architectures. Broadly, our study involves the purposeful addition of defects, which promote electrochemical reactions by increasing the effective area for charge transfer. The layered structure of graphite/multi-walled carbon nanotubes (CNTs), constituted of edge and basal planes, provides an excellent basis for such studies as it is well known[6,7] that edge plane like defects have a electrochemical rate constant of up to five orders of magnitude[8] greater than that of the latter constituent and that their ratio could be manipulated for altering electron transfer kinetics. We indicate that the implications may be more profound in terms of charge configuration and storage, e.g., dangling bonds resident on edge plane like defects may serve for enhancing the charge and energy density. We then explore themes where the fractions of defects resembling the edge plane may be created and relatively easily tuned. CNT arrays were found particularly appealing as they afford a large area over which such effects can be monitored and averaged.

For this purpose, multi-walled CNT arrays were synthesized on electrically conducting silicon wafers through thermal chemical vapor deposition (CVD). The CNTs were subsequently exposed to argon and hydrogen based plasmas, where it was hypothesized that locally charged defects could be created through exposure to ions in the plasma. Such defects would influence the graphitic structure,[9] e.g., through electron and phonon renormalization.[10] A manifestation of charge transfer related to the CNTs was observed in Raman spectroscopy, through shifts in the in-plane vibrational mode, indicative of sp^2 bonding networks, represented by the G-band (∼1580 cm^{-1}) and the defect induced D-band (∼1350 cm^{-1}). The D-band feature fundamentally arises through localized loss of sp^2 symmetry and associated molecular/crystallite formation[11] and was used as a measure (relative to the G-band peak intensity) of the total defect density.[12] We also considered the relative variation of the D' band (at ∼1620 cm^{-1}), a bounding layer mode with high density of electronic states[13] and which has been shown[14,15] to be specifically indicative of the edge planes, as a measure of the edge plane density. We then correlated the extent of edge plane like defects with respect to the total defect density, through monitoring the relative intensity (I) ratios: (I_D/I_G) and ($I_{D'}/I_G$). Observing the relationships between edge plane content and the consequent modulation of the electrical capacitance, through detailed electrochemical measurements, allowed for the investigation of the effects of plasma exposure on electrochemical charge transfer.

Experimental

Materials synthesis and processing.— Substrates for CNT growth were initially prepared by depositing a 5 nm Fe thick catalyst layer (using a Temescal BJD 1800 E-beam evaporator) on 3″ *n*-doped Si wafers (resistivity of ∼1–10 mΩ cm). The wafers were then diced with a Disco Automatic Dicing Saw 3220 into 5 mm × 5 mm squares using a blade with a width of 20 μm. Multi-walled CNT growth was conducted in a thermal CVD system with a 1″ diameter quartz tube and a length of 33″. To initiate the growth process, the Si substrates were placed at the center of the quartz tube and the system was evacuated to less than 100 mTorr to remove atmospheric oxygen, then purged with Argon gas at a flow rate of 350 standard cubic centimeters per minute (SCCM) until a pressure of 750 Torr was reached. The temperature of the furnace was then ramped to 650°C at a rate of 50°C /min. At 650°C, H_2 was introduced into the system at a flow rate of 180 SCCM for 10 min prior to the growth. To initiate CNT growth, 25 SCCM of C_2H_4 was then introduced into the gas mixture for 10 min, while the furnace was held at 650°C.[16] After a designated growth time elapsed, H_2 and C_2H_4 gas flow into the reactor was stopped and the system was allowed to cool to room temperature in an Argon atmosphere. The length, diameter, and separation of the CNTs were measured with a Phillips XL30 environmental scanning electron microscope (ESEM) at multiple locations on the Si wafer before and after post growth processing (as detailed later in the text) with average values determined to be 25 ± 4 μm, 20 ± 5 nm and 150 ± 50 nm, respectively (see Figure 1b). The ESEM was equipped with an Oxford EDS attachment with an energy resolution of 70–130 eV and an elemental detection limit of ∼ 0.1 wt%.[17,18]

The nanotubes were subject to argon and hydrogen gas based plasma treatments, to investigate possible correlations of plasma ambients to induced defect density, as well as possible reactions between ions and the CNTs. The treatments were conducted with a Trion reactive ion etcher (RIE) with an applied electrode bias and added Inductively Coupled Plasma (ICP) power, where the later was used to independently enhance the plasma density.[19–23] For the given experimental setup, the ion density in the plasma was ∼ 10^{11} ions/cm^3 and the DC bias was hypothesized[22] to be between −100 V and −180 V. For such an ion density, the ion energy was estimated to be ∼ 25 eV, similar to those reported elsewhere.[21] The operating pressure and power were chosen to maximize the concentration of specific plasma species.

For argon treatments, a variety of ionization and recombination processes occur in the plasma (as a function of pressure and

[z]E-mail: pbandaru@ucsd.edu

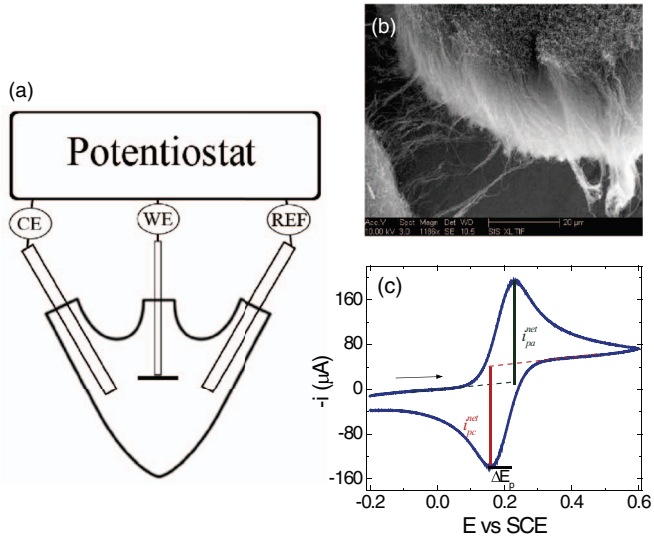

Figure 1. (a) Three electrode cyclic voltammetry based experimental design for CNT working electrode (WE) characterization, which utilized a Pt wire counter electrode (CE) and a saturated calomel reference electrode (REF). (b) SEM image of a typical CNT electrode indicating their length. (c) Linear baseline fitting of CV plot to determine $i_p{}^{net}$ and ΔE_p.

power),[24,25] yet the dominant ion in the gas mixture was Ar^+. Unlike in argon plasmas, several different positively charged species of hydrogen ions can be present depending on the operating pressure,[20,26] thus the processing parameters were chosen such that a majority of only one ion, (say, $H_2{}^+$) was present (i.e., RIE power: 50 W, ICP Power in the range of 0–100 W, pressure: 100 mTorr at 30 SCCM flow rate)

Materials characterization: Raman spectroscopy.— The spectroscopy setup (from Renishaw Inc.) consisted of a 514.5 nm argon laser optically coupled to a microscope and focused on the CNT samples. The grating had 1800 lines/mm, with a microscope objective at 80× magnification, detector exposure time at 30 s, and 2.5 mW of laser power at the sample. Prior to each use, the power at the sample and the calibration of the detector were checked. The calibration was completed by taking a spectra of a polished Si wafer and comparing the experimentally determined peak position to the known value (520.4 cm^{-1}).[27] A normalized intensity value was also calculated and maintained above 1000 counts/mW-s, to maximize the signal-to-noise ratio. The Raman spectra were taken at least five locations on a sample to determine the average G, D, and D' peak positions, peak intensities, and linewidths. All peaks were fit simultaneously using the Levenberg-Marquardt algorithm to minimize the difference (through a chi-square goodness of fit test) between the raw data and the sum of the intensities of the Lorentzian line shapes for each peak. The Lorentzian fit was used instead of a Gaussian line shape since the latter is typically associated with random distributions of phonon lifetimes, whereas the Lorentzian is characteristic of more homogeneous distributions.[28]

Cyclic voltammetry and chronocoulometry.— Cyclic voltammetry (CV) and chronocoulometry (CC) experiments were carried out using a PCI4-300 potentiostat from Gamry Instruments incorporating a three electrode setup (Figure 1a). A saturated calomel electrode (SCE) was used as the reference (REF) electrode. All used chemicals were of purity >97% and were purchased from Sigma-Aldrich Inc. The Pt counter electrode (CE) was polished with micro-bead metal polish and cleaned with Alconox detergent dissolved in deionized water (DI) and sonicated for 2 minutes to ensure full removal of the polish. The majority of experiments were conducted with solutions of the well known redox couple: 10 mM potassium hexacyanoferrate(III) ($K_3Fe(CN)_6$) in 1.0 M aqueous potassium chloride (KCl) supporting electrolyte, in the voltage range of −0.2 to 0.6 V. Specific experiments, for trial and comparison, were also conducted with 10 mM ruthenium hexaamine trichloride ($Ru(NH_3)_6Cl_3$) in 1.0 M KCl and compared to the results with potassium hexacyanoferrate(III) to determine any dependencies on the redox couple. For CV, the voltage scan rates (ν) used were in the range of 25 mV/s to 1 V/s. Any particular CV run consisted of five full cycles. For CC experiments, the applied voltages were similar to those used in the CV, to ensure that the diffusion processes (faradaic) could be separated from any double-layer or adsorption effects. We also carefully looked for and eliminated the possibility of hexacyanoferrate complex adsorbate formation on the electrodes when using $K_3Fe(CN)_6$, through the choice of the voltage scan range and by using freshly prepared (< 2 hours old) solutions.[29]

Prior to any use of the CNTs as the working electrode (WE), CV and CC were conducted using a platinum WE, with a nominal area of 0.071 cm^2, which acted as an ideally non-polarizable electrode. Subsequent experiments were then conducted with CNTs. However, to accurately attribute changes in electrochemical charge transfer processes to changes in the nanostructure, the full CNT surface area must be wetted by the redox couple/KCl_{aq} solution. Due to the hydrophobic nature of as produced (AP) CNTs, the CNT electrodes could not be directly placed into the solution used for CV and CC experiments. Instead the electrodes were sequentially dipped in isopropyl alcohol (30 s), acetone (30 s), and finally 1 M KCl_{aq} (10 min) after which the CNTs were fully wetted with KCl_{aq} and finally contacted with the KCl/redox couple solution. To distinguish between any possible substrate contributions to charge transfer a bare Si wafer was used as a working electrode and the CV curves were compared. For the blank Si wafer, no redox peaks were observed with negligible current relative to that from the CNT electrodes.

Electrochemical characteristics and changes, due to CNT treatment and processing, were quantified through changes in (i) the kinetic parameters: ΔE_p (the difference between the cathodic and the anodic peak potentials in the CV spectra: see Figure 1c) and the standard electrochemical rate constant (k^o), as well as the (ii) the active cross-sectional area (A), normal to the axis of diffusion of the redox species,[16,30] and (iii) adsorption processes. First, the *method of Nicholson*[31] was used to correlate the experimentally recorded ΔE_p to k^o through a dimensionless parameter $\Lambda = k^o\sqrt{RT/DF\nu}$, a measure of the relative rates of kinetic and diffusive processes,[31,32] where R is the gas constant (=8.31 J/mole K), T is the absolute temperature in Kelvin, D is the diffusion coefficient of the oxidized (O) and reduced (R) redox species, assuming D ($=D_O = D_R$), F is the Faraday constant (=96 485 C/mole), and ν the voltage scan rate. The Λ was used to define the boundaries of reversible (Λ>15), quasi-reversible ($15 \geq \Lambda \geq 10^{-3}$) and totally irreversible $\Lambda < 10^{-3}$ electron transfer for the redox couples used in this work.[7]

Second, the *net* peak current ($i_p{}^{net}$) was defined through:[31,33]

$$i_p^{net} = i_p^{ads} + i_p = \frac{n^2F^2}{4RT}\nu A\Gamma^* + \xi(T)n^{3/2}AB^*\sqrt{D\nu}K(\Lambda,\alpha) \quad [1]$$

where the first term, $i_p{}^{ads}$ is the contribution from adsorbed redox species, while the second term: i_p, arises from a modified Randles-Sevcik equation that accounts for deviations away from *ideally reversible* electron transfer for diffusing redox species. In the above, n is the number of electrons transferred (e.g., $n = 1$ for $Fe(CN)_6{}^{3-} + e^- \leftrightarrow Fe(CN)_6{}^{4-}$), $\xi(T)$ is a temperature dependent constant (=2.69 × 10^5 $C/mol\sqrt{V}$ at 298 K), B^* is the bulk concentration of the redox species, Γ^* the concentration of adsorbed redox species, and $K(\Lambda,\alpha)$ is a function used to describe the deviation from ideally reversible electron transfer with an upper limit of unity for completely reversible systems. The α is a transfer coefficient (=0.5 for the considered redox couples).[31]

Finally, CC was utilized to verify any changes in diffusion processes measured through CV. For an initial potential step the *net* charge passed to solution (Q^{net}) was defined through the sum of the charges relevant to (i) diffusion related processes (Q_{diff}), (ii) adsorbed species

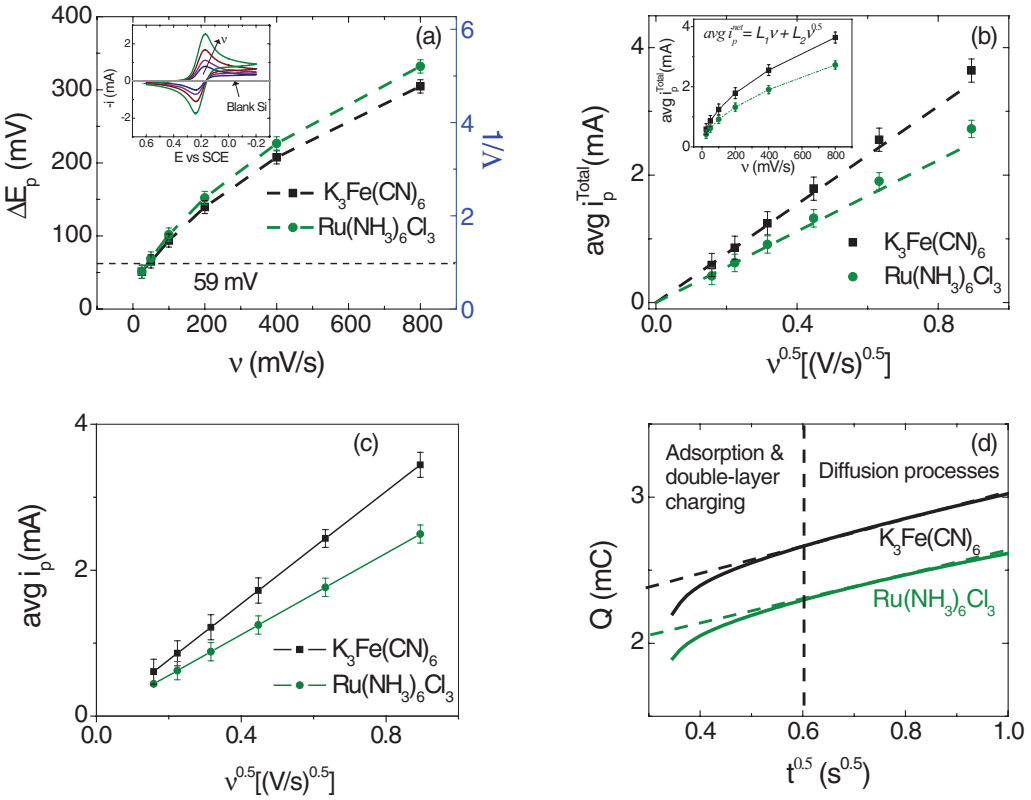

Figure 2. (a) The change in ΔE_p (Λ) – *see text for definitions*, for as produced (AP) CNT working electrodes (WE) when 10 mM $K_3Fe(CN)_6$ and 10 mM $Ru(NH_3)_6Cl_3$ in 1.0 M KCl were used as the redox couples. *Inset*: CV scans for the AP CNTs and for a blank Si wafer - which does not demonstrate any appreciable faradaic response. (b) The positive shift of the average i_p^{net} to values greater than the reversible fit (dashed lines) as ν increases, indicates the presence of adsorbed species. *Inset*: Non-linear fits (dashed lines) of i_p^{net} to ν to separate i_p and i_p^{ads}, (c) Corrected plot of the magnitude of i_p to determine the effective area, A. (d) Typical chronopotentiometry plots for CNT working electrodes. Linear fits to Q_{diff} were used to determine A, as a function of the redox couple, i.e., ~0.51 cm^2 for $K_3Fe(CN)_6$ and 0.50 cm^2 for $Ru(NH_3)_6Cl_3$.

(Q_{ads}), and from (iii) the double-layer (Q_{dl}):[34]

$$Q^{net} = Q_{diff} + Q_{ads} + Q_{dl} = 2nFAB^*\sqrt{Dt/\pi} + nFA\Gamma^* + Q_{dl} \quad [2]$$

Since charge transfer to the adsorbed species (Q_{ads}) and the double layer (Q_{dl}) occur on a relatively shorter time scale than charge transfer arising from diffusion processes, Q_{diff} can be isolated from the effects related to $Q_{dl} + Q_{ads}$ allowing for the computation of A.

As either Equations 1 or 2 can be used for the area (A) computation, for the quantification of the relative accuracy of either approaches and calibration, A was measured for a platinum WE with a nominal, geometrically determined, area of 0.071 cm^2. For all CV experiments, the anodic and cathodic peak voltage separation remained reasonably constant ($\Delta E_p = 73.0 \pm 2.6$ mV, implying $\Lambda \sim 6$) in the given range of scan rates. The $K(\Lambda, \alpha = 0.5) > 0.98$, implying close to reversible electron transfer at the Pt WE. A plot of i_p with respect to $\sqrt{\nu}$ should therefore be linear with a slope equal to $2.69 \times 10^5 n^{3/2} AB^*$. Using the approximation of $D_O = D_R = 6.86 \cdot 10^{-6}$ cm^2/s for 10 mM $K_3Fe(CN)_6$ in 1.0 M KCl,[35] the A was determined to be 0.0677 ± 0.0033 cm^2. Similarly, A was obtained from a plot of Q^{net} as a function of $\sqrt{t}$ for the initial voltage step in CC, with a slope equal to $2nFAB^*\sqrt{D/\pi^5}$, and a corresponding A of 0.0649 ± 0.0080 cm^2. The ~ 5% difference between the areas obtained through CV and CC illustrates that both the methods would be accurate for practically determining the effects of diffusion and adsorption on the surface area of the working electrode.

Results and Discussion

Evaluation of influence of specific redox couple.— The methodology used to evaluate A of the Pt WE, detailed above, was used to determine any potential dependencies on the chosen redox couple for CNT electrodes. ($K_3Fe(CN)_6$) - an inner-sphere redox couple, and ($Ru(NH_3)_6Cl_3$) - an outer-sphere redox couple, and possible sensitivity to surface chemistry.[36] As illustrated in Figure 2a, the ΔE_p is dependent on the scan rate (ν), for both redox couples, indicating a transition to quasi-reversible electron transfer ($1/\Lambda > 0.067$) at the CNT electrodes. Also, at $\nu > 200$ mV/s, a *slight* upward curvature in the plot of i_p^{net} versus $\sqrt{\nu}$ was observed – Figure 2b, indicating possible non-diffusion related processes. It was then hypothesized that both adsorption and diffusion processes may occur for CNT electrodes, as also indicated by ΔE_p values slightly less than 59 mV.[16]

To correct for the effects of adsorption, plots of i_p^{net} as a function of ν were fit to a nonlinear equation of the form:[37] $i_p^{net} = L_1\nu + L_2\sqrt{\nu}$, using the Levenberg-Marquardt algorithm, as depicted in the inset to Figure 2b, where L_1 and L_2 can be approximated as constants following Equation 1. After fitting to the experimental data, the (L_2/L_1) ratio was calculated to determine the relative contribution of i_p^{ads} and i_p to i_p^{net}. As the ratio was determined to be > 10 for all the as prepared (AP) CNT electrode samples, it was deduced that adsorption effects on the peak current are relatively small compared to diffusion based processes. The surface area for electron transfer was then calculated from L_2 to be 0.55 ± 0.01 cm^2 for $K_3Fe(CN)_6$ and 0.53 ± 0.01 cm^2 for $Ru(NH_3)_6Cl_3$. From CC, A was determined to be 0.51 ± 0.03 cm^2 for $K_3Fe(CN)_6$ and 0.50 ± 0.01 cm^2 for $Ru(NH_3)_6Cl_3$ from the plots

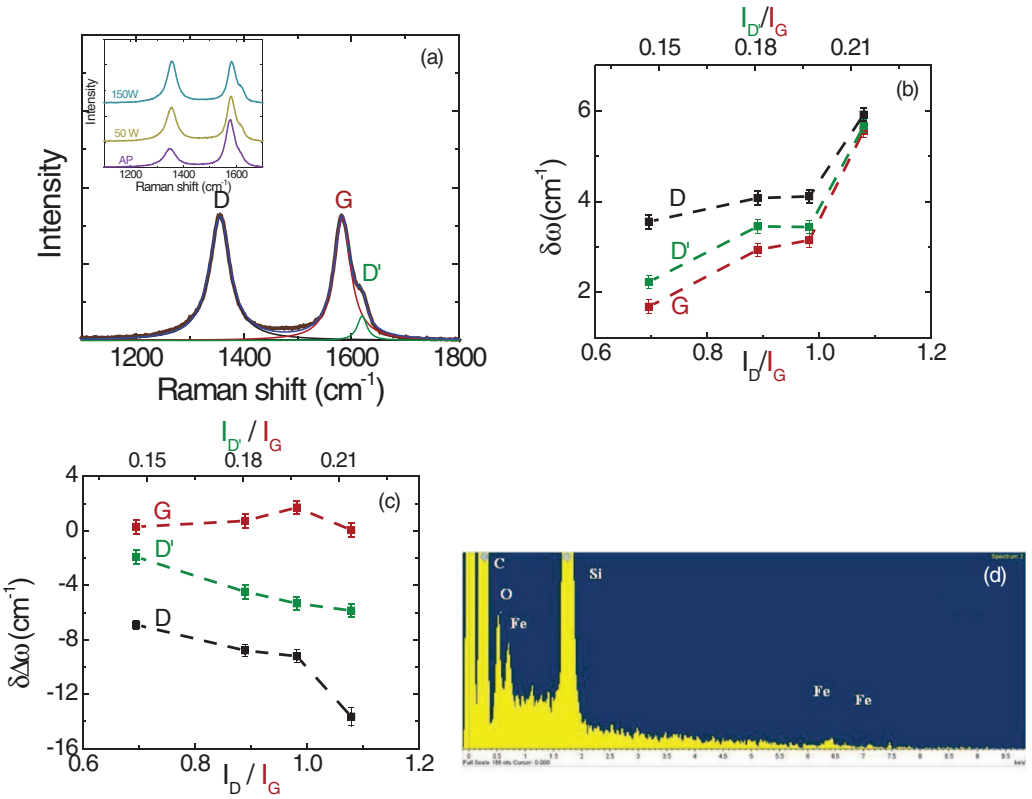

Figure 3. (a) Raman scattering spectra used to infer charge density modulation in defect induced carbon nanotube arrays. The deconvolution and fitting of the observed line shape into the defect induced D- band (represented in black), the in-plane vibrational band (G: red) and the edge plane defect induced D'- (green) bands is shown. (*Inset*: An enhanced D'-band intensity was observed through subjecting the arrays to escalating amounts of inductively coupled plasma power (from the bottom: AP- as prepared, 50 W, and 150 W), (b) The up shifts of the D-, D'-, and G- bands attributed to the removal of carbon atoms and the creation of electroactive chemical reaction sites. The top and bottom axes indicate the ratios of the D' and D peak intensity relative to the G peak intensity, respectively. (c) Change in the peak widths with increasing defect desnity and (d) Lack of Ar in EDS spectra of the CNT electrodes may indicate that Ar is not intercalated into the CNTs.

indicated in Figures 2c and 2d. The small difference in the estimated A between $K_3Fe(CN)_6$ and $Ru(NH_3)_6Cl_3$ demonstrated that the redox couple used had negligible effect on diffusion and charge transfer phenomenon, therefore all subsequent analysis will be discussed with respect to the use of $K_3Fe(CN)_6$ alone.

Increasing the active surface area through Ar plasma exposure.— It was observed through Raman spectroscopy, that on argon plasma exposure (with Ar^+ species), that there was an up-shift ($\delta\omega$) of the G, D, and D' peak frequencies of $\sim 6 \pm 0.2$ cm^{-1} as detected through the deconvolution of the observed Raman spectra (Figure 3a) as illustrated in Figure 3b, indicating charge transfer *from* the CNTs.[38,39] The inset to Figure 3a indicates an enhanced D'-band intensity correlated with increased edge plane like defects observed through subjecting the arrays to escalating amounts of inductively coupled plasma power. The Ar^+ ions may have served to (i) abstract electron density, similar to what has been observed in graphite intercalation compounds (GICs),[40,41] or could be involved in the (ii) removal/sputtering of the C atoms,[42] reducing π-bond conjugation and stiffening the bonds. Using a $\delta\omega/\Delta q$ of $\sim$460 cm^{-1} for strong acceptors,[39] we estimated only one deficit electron/hole existed per 100 C atoms ($1/\Delta q$) yielding an approximate average spacing of 4 nm. The relatively large value of $1/\Delta q$ is contrary to what was expected for intercalated strong acceptors. An alternate evaluation of the average distance between the defects was made through the Tuinstra-Koenig relationship,[12,43] which yielded an average correlation length/defect separation (L_a) of $\sim$5 nm. The fairly good comparison between the two techniques appeared to indicate that charge removal arose at defect locations. Additionally, it was noted that the peak width: $\Delta\omega_G$ did not change significantly (Figure 3c). This is in contrast to what is typically observed in GICs where $\Delta\omega_G$ may increase by up to $\sim 70 \pm 0.2$ cm^{-1} with increasing I_D/I_G.[11,44–47] The presence of Ar was also not detected in the EDS spectra (Figure 3d). Based on the above, we conclude that Ar^+ was most likely not intercalated between the CNT walls.

However, it was noted that in the transition from graphite to microcrystalline graphite there was not a significant $\Delta\omega_G$ change,[11,43] and it is consequently plausible that similar processes are operative here as well. Bond contraction may occur as a result of carbon atom removal/sputtering, leading to a loss of aromaticity and a decrease in π-bond delocalization. Furthermore, the narrowing of $\Delta\omega_D$ and $\Delta\omega_{D'}$ with increases in $I_{D'}/I_G$ indicate that newly formed defects are most likely energetically similar edge-plane like defects.

Edge-plane formation can have an important impact on (a) charge transfer kinetics,[6,8,48] and (b) the number of reaction sites for electrochemical reactions[6,37,49,50] as defects at such locations have intrinsically higher density of states (DOS) relative to the basal plane (due to the presence of dangling bonds) and are thus more reactive.[48,51] Argon treated CNTs exhibited a transition to quasi-reversible electron transfer for scan rates greater than $\sim$100 mV/s as indicated by the increase in $1/\Lambda$ above 0.067 (i.e., $\Lambda < 15$) (Figure 4a). If electron transfer is assumed to be confined to the edge plane and the basal planes, an increase in the edge-plane fraction (θ_{edge}), over the basal-plane fraction (θ_{basal}), is also expected to increase the observed standard rate constant (k^o), through:

$$k^\circ = \theta_{basal} k^\circ_{basal} + \theta_{edge} k^\circ_{edge} \qquad [3]$$

where ($k^o{}_{edge}$/ $k^o{}_{basal}$) is typically[6,48,52] greater than 10^5 and $\theta_{basal} + \theta_{edge} = 1$. An increase in θ_{edge} would therefore allow for a greater

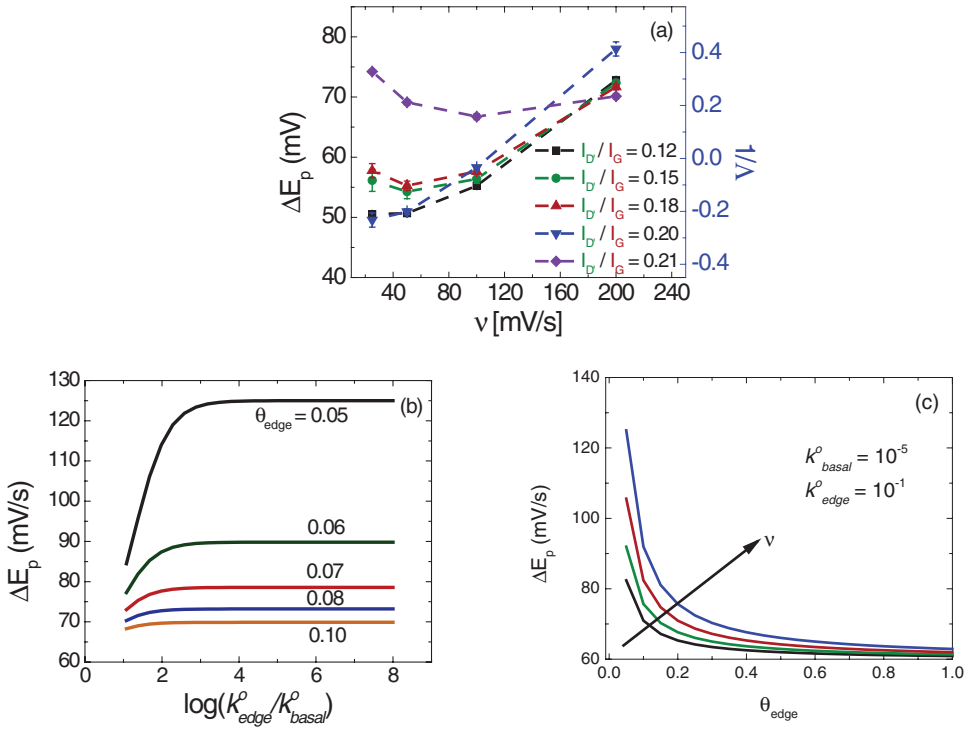

Figure 4. Electrochemical characterization indicates defect induced increase in the effective area of charge transfer and deviations from planar diffusion processes. (a) The variation of the ΔE_p, with ν, at different $\frac{I_{D'}}{I_G}$ ratios indicate quasi-reversible electrode kinetics. Predicted dependence of ΔE_p vs (b) (k^o_{edge}/k^o_{basal}) as a function of θ_{edge} at a scan rate, (ν) of 200 mV/s, and vs (c) θ_{edge} as a function of ν used in the experiments.

range of ν to be employed while maintaining reversible electron transfer (yielding a ΔE_p of $\sim$ 59 mV). However, an unexpected increase in ΔE_p to values greater than 70 mV was observed, which was attributed to $\theta_{edge} < 0.10$ for the scan rates used, assuming a range of (k^o_{edge}/k^o_{basal}) as depicted in Figures 4b and 4c. A relatively small fraction of edge planes relative to the basal plane is then expected, since the majority of the CNT structure would be comprised of basal planes.

The effect of quasi-reversibility on $i_p{}^{net}$ at scan rates greater than 100 mV/s is relatively small since $K(\Lambda, \alpha = 0.5)$ was typically greater than 0.96. Furthermore, ($i_p/i_p{}^{ads}$) >25 for the scan rates used, and thus the contribution of $i_p{}^{ads}$ to the net current is less than 4% of the total current and was consequently considered negligible. As i_p scales proportionally to $\sqrt{\nu}$, A was calculated from the slope of the plot (Figure 5a). The change in area (ΔA) with respect to the effective, original, surface area of the AP CNTs (A_0) as a function of the change in $I_{D'}/I_G$ ratio is shown in Figure 5b. Induced edge-plane defects seem to appear as new sites for electron transfer, for a given projected area of the sample size. Such an increase in the active area for charge transfer increases energy density through an increase in the faradaic current, and is applicable for both battery and capacitor architectures.

While the values of the capacitance C_p ($=i_p/\nu$, where i_p is the peak current following equation 1), can be computed from the data of Figure 5, we do not report the specific values. The rationale is that, typically, the values of C_p are considered in units of capacitance/unit area (i.e., F/m^2) or capacitance/unit weight (i.e., F/g). However, both the area and the weight are uncertain and susceptible to error for reasons related to whether the effective area relates to the total or the projected area, and which could also vary with plasma processing. We mention that the variation of the computed C_p follows closely the i_p variation, as depicted in Figure 5b, and that the net increase in capacitance (ΔC_p) with argon plasma processing could be in the mF range.

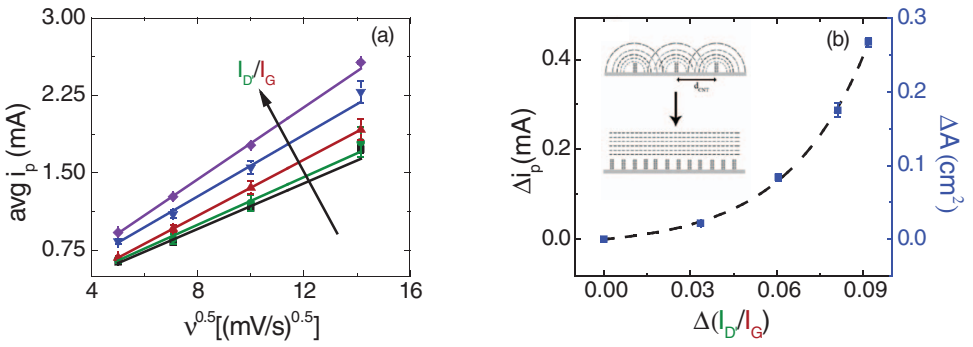

Figure 5. (a) The peak current (i_p) varied linearly with $\sqrt{\nu}$. (b) A large increase and change (Δi_p) in the faradaic current, was obtained through the exposure of the CNT electrodes to argon plasma. An equivalent change in the area (ΔA) was estimated from the CV and confirmed through CC. The enhancement in the area is *unusual*. *Inset:* It is expected that as the distance between the individual electrodes is reduced (relative to the diffusion distance) that the diffusion fields would overlap, transitioning (indicated from top → bottom) to a planar electrode like behavior.

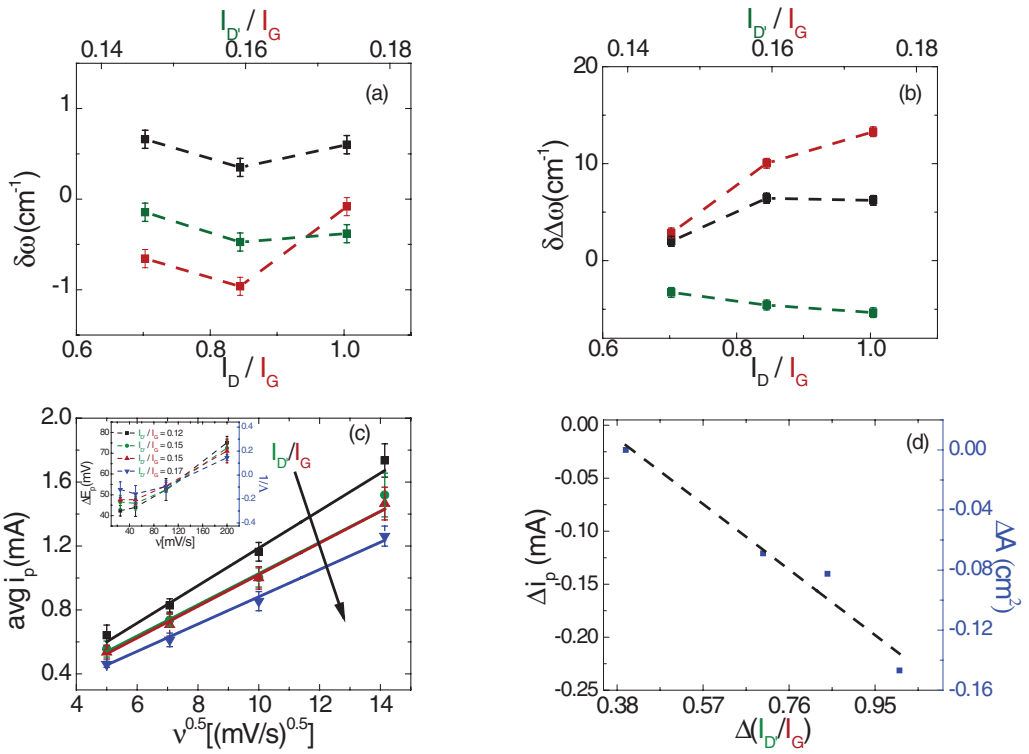

Figure 6. On exposure of the CNT electrodes to hydrogen plasma, there was observed a lack of (a) peak shifts and (b) peak widths in the Raman spectra. (c) The peak current (i_p) from CV, varied linearly with $\sqrt{\nu}$. *Inset:* An increase in ΔE_p indicates quasi-reversible electron transfer. (d) A decrease and change (Δi_p) in the faradaic current, was obtained and yielded an equivalent decrease in the area (ΔA), as estimated from the CV and confirmed through chronocoulometry.

In a heterogeneous system comprised of individual electrodes (i.e., the CNTs) of diameters and spacing less than the diffusion layer thickness, $\delta(\sim \sqrt{\pi D \Delta E/\nu})$, the general understanding[7,31] is that the diffusion layers from each electrode would overlap resulting in planar diffusion. For example, with a ΔE of ~0.4 V and ν~100 mV/s, the δ was estimated to be ~ 100 μm, much greater than the spacing between CNTs (~ 150 nm) and manifest macro electrode like behavior.[6,31] Consequently, the CNT constituted electrode array should behave as a planar electrode with an effective area equal to the projected area.[7] However, it was noted that the estimated A calculated from the relationship for i_p was greater than the projected area of a typical sample (wafer diced to 0.25 cm^2). Noting that the relation was derived assuming semi-infinite linear diffusion equations with flux balance of species at the electrode interface, the obtained A would then seem to imply *non-planar* diffusion processes. Such aspects could also be inferred through the increases in i_p with Ar^+ exposure at a specific ν, implying sensitivity of electron transfer to microscopic defect structures in the CNTs.

A possible mechanism for the changes in effective charge transfer area while maintaining θ_{edge} below 0.1 could arise from macroscopic changes in the surface roughness of the CNT forest. However, there were no observed visual changes in the CNT geometry as observed through SEM, subsequent to processing over the range of used parameters. We instead surmise that the changes in the number of reactions sites is directly related to changes in the fraction of reactive edge planes, which will be further established when evaluating the effects of hydrogen plasma exposure.

Reaction site reduction through hydrogen plasma treatments.— Alternately, exposure of the CNTs to hydrogen plasmas, which under the investigated conditions mostly consisted of H_2^+ ions,[20,26] resulted in a net reduction of i_p, despite an increase in $I_{D'}/I_G$. From a structural viewpoint, it was seen through Raman spectroscopy that the G, D, and D'- peak positions were unchanged (Figure 6a), possibly implying concurrent processes of defect creation and passivation. Moreover, the increased widths of the G and D-bands (Figure 6b) may imply the uptake of hydrogen into the nanotubes.[53,54] In this context, hydrogenation reactions may occur during hydrogen plasma exposure, passivating defects/dangling bonds.[55] Based on the above, we ascribe the reduction in i_p to charged defect passivation by hydrogen. The observation of the linear variation of i_p coupled with a change in ΔE_p with ν indicates quasi-reversible electrode kinetics, where the deviation from reversibility was deemed to be relatively small as seen by $K(\Lambda, \alpha = 0.5) \sim 1$. The relative effect of i_p^{ads} on i_p^{net} was once again minimal, as the (i_p/i_p^{ads}) ratio was greater than 35. Since ΔE_p does not increase significantly with defect passivation, as would be expected if the reaction site density were significantly reduced (*cf*, Figures 4b and 4c), the reaction site passivation seems to be *offset* by creation of new reaction sites through defect creation and thus only slightly decreases with increasing H_2^+ exposure as demonstrated in Figure 6c. In H_2^+ ion exposed nanotubes, there is consequently now a *decrease* in the effective area, A – Figure 6d. The charged defects in nanotubes may have been passivated through interaction with H_2^+ ions in the plasma, concomitant with diminished capacitance and reduced electroactive reaction site area. Following the previous discussion related to the *increase* of the capacitance due to argon plasma processing, the exposure of the CNTs to hydrogen plasmas results in a net *reduction* of the i_p and C_p, i.e., a ΔC_p reduction of the order of ~ 5 mF corresponding to the i_p variation in Figure 6d.

Summary

The results from the present work then bring forth new principles whereby defect induced charges[56,57] and passivation may be used to affect the local charge of a structure from the microscale upwards, as schematically illustrated in Figure 7. Detailed statistical analyzes of the width as well as the intensity of selective spectral features in Raman spectroscopy, i.e., related to the G, D, and D' peaks, have indicated the influence of argon and hydrogen based plasma processing, e.g., where the upward shift of the peak frequencies of ~ 6 cm^{-1} implies charge

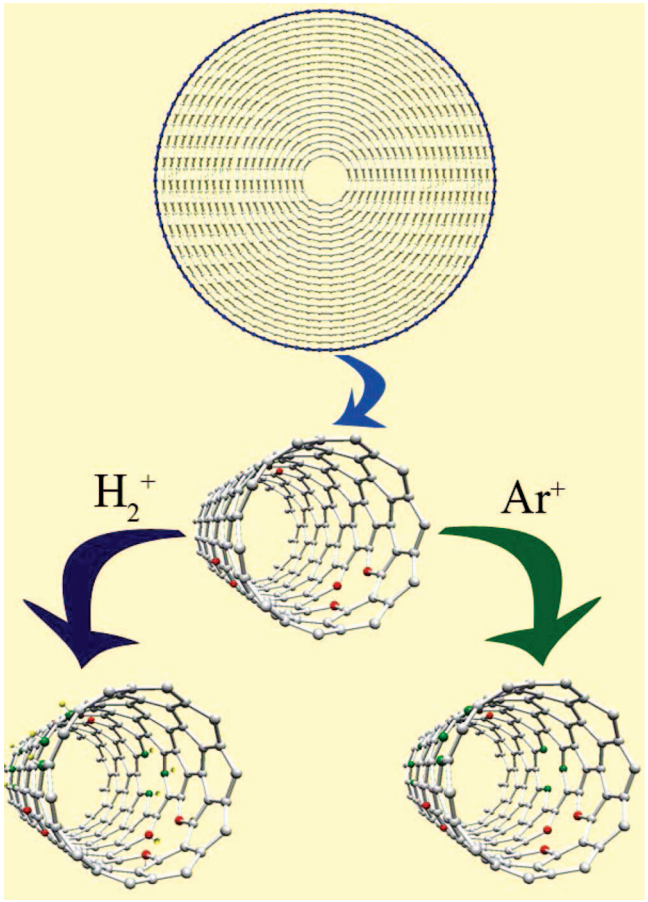

Figure 7. Schematic of the influence of intrinsic and extrinsic structural defects in multi-walled carbon nanotubes. The intrinsic defects (green) in a multi-walled CNT may contribute to charged dangling bonds and edge-plane like defects (a single wall is shown for clarity), the density of which could be increased through exposure to argon plasmas (such extrinsically introduced defects are shown in red). A degree of control may be achieved through passivation of the defects through exposure to hydrogen plasma, due to the attachment of hydrogen atoms (shown in yellow).

transfer from the nanotubes. Concomitant effects from the plasma processing are implicated in the *increase/decrease* of the effective area for electrochemical reactions, facilitating tunable electrochemical response, e.g., with argon plasma exposure, the effective area of charge transfer could be reproducibly increased by ∼100% (0.25 cm^2 to ∼0.50 cm^2), while exposure to hydrogen based plasmas resulted in decrease in the effective area by nearly 60% (0.25 cm^2 to ∼0.10 cm^2). Such conclusions have been independently verified to an accuracy of ∼ 5% through both cyclic voltammetry and chronocoulometry, considering the effects of diffusion and adsorption. It has also been indicated that a net increase/decrease in capacitance of the order of mF could be accomplished through argon/hydrogen plasma processing, respectively. Such considerations would be integral to enhancing the energy storage density of electrochemical energy storage devices.[58–60]

Acknowledgments

This work was supported by the US National Science Foundation under grant ECS-0643761. The authors thank J. Nichols for his assistance in the initial experiments. The authors are grateful to Professor Frank Talke for the use of the Raman spectrometer and Dr. B. Fruhberger and R. Anderson for assistance in synthesis and sample fabrication.

References

1. D. Linden and T. B. Reddy, *Linden's Handbook of Batteries*, McGraw Hill, New York, NY (2010).
2. J. B. Goodenough, Basic Research needs for electrical energy storage (Department of Energy), in *Report of the basic energy sciences workshop on electrical energy storage*, Washington D.C. (2007).
3. P. Simon and Y. Gogotsi, *Nature Materials*, **7**, 845 (2008).
4. A. F. Burke, in *Linden's Handbook of Batteries*, T. B. Reddy and D. Linden Editors, McGraw Hill, New York, NY (2011).
5. B. E. Conway, *Electrochemical Supercapacitors; Scientific Fundamentals and Technological Applications*, Kluwer Academic/Plenum Publishers, New York (1999).
6. C. E. Banks, T. J. Davies, G. G. Wildgoose, and R. G. Compton, *Chem. Commun.*, **7**, 829 (2005).
7. R. G. Compton and C. E. Banks, *Understanding Voltammetry*, Imperial College Press, London, UK (2011).
8. R. J. Rice and R. L. McCreery, *Analytical Chemistry*, **61**, 1637 (1989).
9. M. A. Pimenta, G. Dresselhaus, M. S. Dresselhaus, L. Cancado, A. Jorio, and R. Saito, *Physical Chemistry and Chemical Physics*, **9**, 1276 (2007).
10. I. O. Maciel, N. Anderson, A. Jorio, M. A. Pimenta, M. A. Hartschuh, H. Qian, M. Terrones, H. Terrones, J. R. C. Delgado, and A. M. Rao, *Nature Materials*, **7**, 878 (2008).
11. J. Robertson, *Materials Science and Engineering R*, **37**, 129 (2002).
12. F. Tuinstra and J. L. Koenig, *Journal of Chemical Physics*, **53**, 1126 (1970).
13. M. S. Dresselhaus and G. Dresselhaus, *Advances in Physics*, **51**, 1 (2002).
14. L. G. Cancado, M. A. Pimenta, B. R. A. Neves, M. S. S. Dantas, and A. Jorio, *Phys. Rev. Lett.*, **93**, 247401 (2004).
15. L. Malard, M. Pimenta, G. Dresselhaus, and M. Dresselhaus, *Physics Reports*, **473**, 51 (2009).
16. M. Hoefer and P. R. Bandaru, *Journal of Applied Physics*, **108**, 034308 (2010).
17. http://www.x-raymicroanalysis.com/x-ray-micro (2012).
18. P. Kuisma-Kursula, *X-Ray Spectrometry*, **29**, 111 (2000).
19. J. Hopwood, *Plasma Sources Science and Technology*, **1**, 109 (1992).
20. S. Nunomura and M. Kondo, *Journal of Applied Physics*, **102**, 093306 (2007).
21. N. Sadeghi, M. van de Grift, D. Vender, G. M. W. Kroesen, and F. J. de Hoog, *Applied Physics Letters*, **70**, 835 (1997).
22. J. Lee, J. F. Donohue, K. D. Mackenzie, R. Westerman, D. Johnson, and S. J. Pearton, *Solid State Electronics*, **43**, 1769 (1999).
23. E. Meeks and J. W. Shon, *IEEE Transactions on Plasma Science*, **23**, 539 (1995).
24. H. Kazumi and K. Tago, *Japanese Journal of Applied Physics*, **34**, 2121 (1995).
25. U. Kelkar, M. Gordon, L. Roe, and Y. Li, *Journal of Vacuum Science & Technology A: Vacuum, Surfaces, and Films*, **17**, 125 (1999).
26. O. Fukumasa, R. Itatani, S. Saeki, K. Osaki, and S. Sakiyama, *Physics Letters A*, **100**, 186 (1984).
27. A. Kolobov, *Journal of Applied Physics*, **87**, 2926 (2000).
28. A. C. Ferrari and J. Robertson, *Physical Review B*, **61**, 14095 (2000).
29. C. M. Pharr and P. R. Griffiths, *Analytical Chemistry*, **69**, 4673 (1997).
30. M. Hoefer and P. R. Bandaru, *Physical Review Letters (in review)* (2012).
31. A. J. Bard and L. R. Faulkner, *Electrochemical Methods: fundamentals and Applications*, John Wiley, New York (2001).
32. H. Matsuda and Y. Ayabe, *Zeitschrift für Elektrochemie, Berichte der Bunsengesellschaft für physikalische Chemie*, **59**, 494 (1955).
33. J. E. B. Randles, *Transactions of the Faraday Society*, **44**, 322 (1948).
34. F. Anson, J. Christie, and R. Osteryoung, *Journal of Electroanalytical Chemistry and Interfacial Electrochemistry*, **13**, 343 (1967).
35. S. J. Konopka and B. McDuffie, *Analytical Chemistry*, **42**, 1741 (1970).
36. X. B. Ji, C. E. Banks, A. Crossley, and R. G. Compton, *Chemical Physics and Physical Chemistry*, **7**, 1337 (2006).
37. M. Hoefer and P. R. Bandaru, *Appl. Phys. Lett.*, **95**, 183108 (2009).
38. A. M. Rao, P. C. Eklund, S. Bandow, A. Thess, and R. E. Smalley, *Nature*, **388**, 497 (1997).
39. P. C. Eklund, E. T. Arakawa, J. L. Zaretsky, W. A. Kamitakahara, and G. D. Mahan, *Synthetic Metals*, **12**, 97 (1985).
40. M. S. Dresselhaus, G. Dresselhaus, M. A. Pimenta, and P. C. Eklund, in *Analytical Applications of Raman Spectroscopy*, M. J. Pelletier Editor, p. 367, Blackwell Science Ltd., Malden (1999).
41. M. S. Dresselhaus, G. Dresselhaus, M. A. Pimenta, and P. C. Eklund, *Analytical Applications of Raman Spectroscopy*, Blackwell Science Malden, MA, (1999).
42. C. Wilkinson and R. Rahman, *Philosophical Transactions of the Royal Society London A*, **362**, 125 (2004).
43. D. S. Knight and W. B. White, *J. Mater. Res.*, **4**, 385 (1989).
44. M. S. Dresselhaus and G. Dresselhaus, *Advances in Physics*, **30**, 139 (1981).
45. B. Elman, M. S. Dresselhaus, M. Shayegan, H. Mazurek, and G. Dresselhaus, *Physical Review B*, **25**, 4142 (1982).
46. B. Elman, M. S. Dresselhaus, G. Dresselhaus, E. Maby, and H. Mazurek, *Physical Review B*, **24**, 1027 (1981).
47. P. Kwizera, A. Erbil, and M. Dresselhaus, *Carbon*, **19**, 144 (1980).
48. R. L. McCreery and M. T. McDermott, *Analytical Chemistry*, **84**, 2602 (2012).
49. R. J. Bowling, R. T. Packard, and R. L. McCreery, *Journal of the American Chemical Society*, **111**, 1217 (1989).
50. T. J. Davies, M. Hyde, and R. Compton, *Angewandte Chemie International Edition*, **117**, 5251 (2005).
51. Y. Niimi, T. Matsui, H. Kambara, K. Tagami, M. Tsukada, and H. Fukuyama, *Physical Review B*, **73**, 085421 (2006).
52. C. C. M. Neumann, C. Batchelor-McAuley, C. Downing, and R. G. Compton, *Chemistry – A European Journal*, **17**, 7320 (2011).

53. A. C. Dillon, K. M. Jones, T. A. Bekkedahl, C. H. Kiang, M. J. Bethune, and M. J. Heben, *Nature*, **386**, 377 (1997).
54. S. Orimo, T. Matsushima, H. Fujuii, T. Fukunaga, and G. Majer, *Journal of Applied Physics*, **90**, 1545 (2001).
55. R. Besser, X. Ouyang, and H. Surangalikar, *Chemical Engineering Science*, **58**, 19 (2003).
56. A. V. Krasheninnikov, K. Nordlund, M. Sirvio, E. Salonen, and E. Keinonen, *Phys. Rev. B: Condens. Matter*, **63**, 245405 (2001).
57. F. Banhart, J. Kotakoski, and A. V. Krasheninnikov, *ACS Nano*, **5**, 26 (2011).
58. T. Brezesinski, J. Wang, S. H. Tolbert, and B. Dunn, *Nature Materials*, **9**, 146 (2010).
59. D. Pech, M. Brunet, H. Durou, P. Huang, V. Mochalin, Y. Gogotsi, P.-L. Taberna, and P. Simon, *Nature Nanotechnology*, **5**, 651 (2010).
60. S. W. Lee, N. Yabuuchi, B. M. Gallant, S. Chen, B.-S. Kim, P. T. Hammond, and Y. Shao-Horn, *Nature Nanotechnology*, **5**, 531 (2010).